AIAA 2001-3588

Exact Self-Similarity Solution of the Navier-Stokes Equations for a Deformable Channel with Wall Suction or Injection

E. C. Dauenhauer and J. Majdalani
Marquette University
Milwaukee, WI 53233

37th AIAA/ASME/SAE/ASEE Joint Propulsion Conference and Exhibit
8–11 July 2001, Salt Lake City, UT

Exact Self-Similarity Solution of the Navier-Stokes Equations for a Deformable Channel with Wall Suction or Injection

E. C. Dauenhauer* and J. Majdalani†
Marquette University, Milwaukee, WI 53233

This paper describes a self-similarity solution of the Navier-Stokes equations for a laminar, incompressible, and time-dependent flow that arises in the context of a deforming channel with permeable walls. The case considered here pertains to a channel that exhibits either injection or suction across two opposing porous walls while undergoing uniform expansion or contraction. Instances of direct application include the modeling of pulsating diaphragms, sweat cooling or heating, isotope separation, filtration, paper manufacturing, irrigation, and the grain regression during solid propellant combustion. To start, the Stokes' stream function and the vorticity equation are used in concert to yield a partial differential equation that lends itself to a similarity transformation in both space and time. Following this similarity transformation, the original problem is reduced to solving a fourth-order differential equation in one similarity variable η that combines both space and time dimensions. Since two of the four auxiliary conditions are of the boundary value type, a numerical solution becomes dependent upon two initial guesses. In order to achieve convergence, the governing equation is first transformed into a function of three variables: the two guesses and η. At the outset, a suitable numerical algorithm that is based on Runge-Kutta integration is applied by solving the resulting set of twelve first-order ODEs with two unspecified start-up conditions. In seeking the two unknown initial guesses, the rapidly converging inverse Jacobian method is applied in an iterative fashion. Numerical results are later used to gain a better understanding of the flow character. The numerical scheme enables us to extend the solution range to physical settings not considered in previous studies. It also broadens the scope to cover both suction and injection concurrently with wall motion.

I. Introduction

HEREIN we present the details of a procedure that can lead to an exact similarity solution of the Navier-Stokes equation in semi-infinite rectangular channels with porous and uniformly expanding or contracting walls. The solution to be developed provides the means to fully characterize the flow field established in such a physical setting. One of the objectives is to extend our current knowledge of laminar flows involving channels with porous walls to encompass moving boundaries.

Laminar flow studies in permeable walls have received considerable attention in the past due to their relevance to a number of engineering applications. These include binary gas diffusion, filtration, ablation cooling, surface sublimation, grain regression (as in the case of combustion in rocket motors), and the modeling of air and blood circulation in the respiratory system.

The earliest studies of steady flows across permeable and stationary walls can be traced back to Berman;[1] therein, Berman investigated the laminar, two-dimensional flow of a viscous incompressible fluid driven by uniform injection (or suction) in a rectangular channel with porous walls. In that study, Berman[1] assumed that the transverse velocity component was independent of the streamwise coordinate. He thus reduced the Navier-Stokes equations to a single, nonlinear, fourth-order, ordinary differential equation (ODE) with four boundary conditions and a cross-flow Reynolds number R. The latter was based on the normal injection speed v_w and channel half-spacing $a(t)$. For small R, he employed a regular perturbation scheme to derive an asymptotic formulation. Numerous studies of channel flows with permeable walls followed. These include the works of Sellars,[2] Terrill[3] (who extended Berman's small R case), Proudman[4]

*Student Member AIAA.
†Assistant Professor, Department of Mechanical and Industrial Engineering. Member AIAA.

(who investigated the large R case using an integral approach), Morduchow[5] (who applied the method of averages over the full injection range), White *et al.*[6] (who provided a convergent power series solution for arbitrary R), Taylor,[7] and Yuan[8] (who provided asymptotic solutions for the infinite and large injection cases, respectively). Improvements to the latter were provided by Terrill.[9]

For unsymmetrical flows caused by different wall velocities, Terrill and Shrestha[10] constructed a generalized perturbation series for small R. For large injection, Shrestha and Terrill[11] extended Proudman's one-term expression using matched asymptotic expansions. In the same vein, Cox[12] considered the practical case of an impermeable wall opposing a transpiring wall.

Treatments of moving boundaries can be traced back to Brady and Acrivos;[13] their endeavor has led to an exact solution of the Navier-Stokes equations for a flow driven by an axially accelerating surface velocity and symmetric boundary conditions. Their work was motivated by the need to study long slender droplets trapped in extensional flows. This effort was made more general by Watson *et al.*[14] who allowed the accelerating walls to be porous. Watson[15] also examined the case of asymmetrically accelerating walls.

In validating the similarity solutions recounted above, investigators have often relied on numerical simulations. Experimental verifications have also been accomplished. In fact, countless laboratory experiments on porous channel flows have been conducted by Taylor,[7] Varapaev and Yagodkin,[16] Raithby and Knudsen,[17] and Sviridenkov and Yagodkin.[18]

The addition of time-dependent motion in a long rectangular channel with porous walls was achieved experimentally by Ma *et al.*[19,20] and Barron *et al.*[21] In fact, both used the sublimation process of carbon dioxide to simulate the injection process at the walls. As a result, the walls of their channel expanded during the sublimation process. Other physical settings that can be modeled with expanding permeable walls include the regression of the burning surface in solid rocket motors and the pulsation of porous diaphragms.

In simulating the laminar flow field in cylindrical solid rocket motors, Goto and Uchida[22] have analyzed the laminar incompressible flow in a semi-infinite porous pipe whose radius varied with time. The present treatment extends their analysis to expanding or contracting channels with porous walls.

II. Formulation

We consider an elongated rectangular channel exhibiting a sufficiently large aspect ratio of width w to height a ($w/a > 4$). Despite the channel's finite body length, it is commonplace to assume semi-infinite length in order to neglect the influence of the opening at the end.[23] The head-end, on the other hand, is closed by a solid membrane; this membrane is allowed to stretch with channel expansions or contractions. As shown in Fig. 1, the axial flow is zero at the closed end ($x = 0$). With x indicating the axial direction and y the normal direction, the corresponding axial and transverse velocity components are defined as u and v, respectively. In this two-dimensional notation, the equations governing the unsteady flow of an incompressible fluid are the differential expressions for mass and momentum conservation. These are given by

$$\frac{\partial u}{\partial x} + \frac{\partial v}{\partial y} = 0 \tag{1}$$

$$\frac{\partial u}{\partial t} + u\frac{\partial u}{\partial x} + v\frac{\partial u}{\partial y} = -\frac{1}{\rho}\frac{\partial p}{\partial x} + \nu\left(\frac{\partial^2 u}{\partial x^2} + \frac{\partial^2 u}{\partial y^2}\right) \tag{2}$$

$$\frac{\partial v}{\partial t} + u\frac{\partial v}{\partial x} + v\frac{\partial v}{\partial y} = -\frac{1}{\rho}\frac{\partial p}{\partial y} + \nu\left(\frac{\partial^2 v}{\partial x^2} + \frac{\partial^2 v}{\partial y^2}\right) \tag{3}$$

where ρ, p, ν, and t are the dimensional density, pressure, kinematic viscosity, and time. The channel walls of interest regress or contract only in the normal direction. Hence, their separation is a function of time. Under the porous wall stipulation, the fluid is injected or extorted uniformly and orthogonally through the channel walls at an absolute velocity v_w. The latter can be shown, in some applications, to be proportional to the expanding wall surface velocity. The boundary conditions necessary for solving the continuity and momentum equations are, as usual

$$u = 0 \qquad v = -v_w \,;\, y = a(t) \tag{4}$$

$$\frac{\partial u}{\partial y} = 0 \qquad v = 0 \,;\; y = 0 \tag{5}$$

$$u = 0 \,;\; x = 0 \tag{6}$$

According to our adopted nomenclature, it should be noted that v_w will be positive for injection and negative for suction. Moreover, we assume that the absolute inflow velocity v_w is independent of position. This implies that the fluid injection speed v_b relative to the wall must be spatially uniform by virtue of the

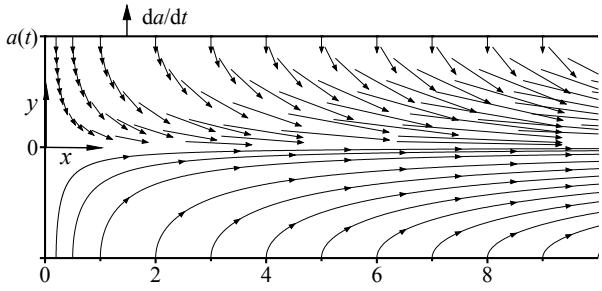

Fig. 1. Coordinate system and bulk fluid motion.

fundamental relation $v_w \equiv v_b - \dot{a}$. Seemingly, a contracting wall (with negative $\dot{a}$) has the same effect on the fluid as that of injection: It can increase the absolute injection velocity (or reduce the suction velocity) at the wall. In the hypothetical case of rigid walls, the relative fluid permeation speed with respect to the walls will be zero and the absolute injection velocity will be equal to $-\dot{a}$. The converse is true for expansion since regression has the same effect as suction at the walls. While v_w and $\dot{a}$ may be independent in nonreactive experiments, they are related, in active propellants, by the solid-to-gas density ratio. This can be explained by referring to the mass conservation equation at the propellant-gas interface. If we let ρ_s be the propellant density, then conservation of mass at the burning surface requires that $\rho A_b v_b = \rho_s A_b \dot{a}$, where A_b represents the burning area. The gas velocity with respect to the wall can therefore be deduced to be

$$v_b = (\rho_s / \rho)\dot{a} \equiv r_\rho \dot{a} \tag{7}$$

where r_ρ is the solid-to-gas density ratio. From Eq. (7) the absolute velocity is observed to be a function of the deformation speed $\dot{a}$ via $v_w = (r_\rho - 1)\dot{a} = A\dot{a}$, where $A = r_\rho - 1$ is the injection coefficient.[22] Since $A = v_w / \dot{a}$, it can be estimated in rocket motors to be $A \sim r_\rho \sim 100$ for a typical $\rho_s \sim 2000 \text{kg.m}^{-3}$ and $\rho \sim 20 \text{kg.m}^{-3}$. Clearly, the injection coefficient A is a measure of the porosity of the wall and can be utilized as a control parameter in the final solution.

By applying mass conservation to a volume ϑ of fluid extending from the closed end ($x = 0$) to an arbitrary location x, the mean flow velocity $u_m(x)$ can be found to be proportional to x. To that end, the mean flow velocity u_m must be determined from

$$u_m(x,t) = \left(\int_{A_c} \boldsymbol{u} \cdot \mathrm{d}\boldsymbol{A} \right) / A_c \tag{8}$$

where $A_c = 2aw$ is the surface area of the cross section. However, since $A_b = 2xw$ is the channel's porous area, conservation of mass in integral form requires that

$$\frac{\partial}{\partial t} \int_\vartheta \rho \, \mathrm{d}\vartheta + \rho A_b v_b - \int_{A_c} \rho \boldsymbol{u} \cdot \mathrm{d}\boldsymbol{A} = 0 \tag{9}$$

where $\mathrm{d}\vartheta = A_c \, \mathrm{d}x$. By virtue of Eq. (8), Eq. (9) becomes

$$\rho x \frac{\partial A_c}{\partial t} + \rho A_b v_b - \rho A_b u_m = 0 \tag{10}$$

wherefore

$$u_m = \frac{A_b}{A_c} v_b - \frac{x}{A_c} \frac{\partial A_c}{\partial t} = \frac{x}{a}(v_b - \dot{a}) = \frac{x}{a} v_w \tag{11}$$

It can be inferred from Eq. (11) that the mean velocity $u_m(x,t)$ varies linearly with x. The choice of a self-similarity transformation that can produce such a variation is therefore desirable. Such a transformation will be presented next. But first, we find it convenient to introduce the Stokes stream function and, thereby, allow the replacement of the two velocity components with a single function such that

$$u = \frac{\partial \psi}{\partial y} \text{ and } v = -\frac{\partial \psi}{\partial x} \tag{12}$$

By definition of the stream function, the continuity equation is self-satisfied and thus no longer useful in determining ψ.

A new variable can now be removed at the expense of introducing another. In fact, the vorticity transport equation for the given geometry can be arrived at by taking the curl of the momentum equation. This operation eliminates the pressure from the momentum equation and introduces, in its stead, the flow vorticity. This is illustrated below. Starting with

$$\nabla \times \left(\frac{D\vec{V}}{Dt} = -\frac{1}{\rho} \cdot \nabla p + \nu \nabla^2 \vec{V} \right) \tag{13}$$

one gets $$\frac{\partial \zeta}{\partial t} + u\frac{\partial \zeta}{\partial x} + v\frac{\partial \zeta}{\partial y} = \nu \left(\frac{\partial^2 \zeta}{\partial x^2} + \frac{\partial^2 \zeta}{\partial y^2} \right) \tag{14}$$

where $$\zeta = \frac{\partial v}{\partial x} - \frac{\partial u}{\partial y} \tag{15}$$

III. Mathematical Procedure

A. Similar Solution in Space

A similar solution with respect to x can be developed due to mass conservation and the fact that the channel height remains constant in the axial direction. In view of the boundary conditions given by Eqs. (4)-(5), one can assume

$$\psi = \nu x G(a) F(\eta, t), \text{ where } \eta = \frac{y}{a} \tag{16}$$

and $F(\eta,t)$ is independent of the axial coordinate. Placing Eq. (16) into Eq. (12), the axial and normal velocities can be expressed in terms of F. One finds

$$u = \frac{\nu x}{a} G(a) F_\eta \quad v = -\nu G(a) F(\eta, t) \tag{17}$$

where $F_\eta = \partial F / \partial \eta$. At this point, one may realize that $u_{xx} = v_x = 0$ and revisit the vorticity equation. Therein, the association $G(a) = 1/a$ can be determined in a manner to insure dimensional homogeneity of the inertial and viscous terms. With this realization, the axial and transverse velocities can be written in their final form, namely,

$$u = \frac{\nu x}{a^2} F_\eta \text{ and } v = -\frac{\nu}{a} F(\eta, t) \tag{18}$$

Noting that the normal velocity v is independent of x, the vorticity equation reduces to $\zeta = -\partial u / \partial y$. Likewise, Eq. (3) becomes $p_{yx} = 0$. Upon substitution of ζ and Eq. (1) into the vorticity transport expression (given by E q. (14)), one obtains

$$u_{yt} + uu_{yx} + vu_{yy} = \nu u_{yyy} \tag{19}$$

Then, by inserting the velocity expression from Eq. (18) into Eq. (19), one develops a differential equation for the main characteristic function F. The result is

$$\left[F_{\eta\eta\eta} + FF_{\eta\eta} + F_{\eta}\left(2\alpha - F_{\eta}\right) + \alpha\eta F_{\eta\eta} - \frac{a^2}{\nu}F_{\eta t}\right]_{\eta} = 0 \tag{20}$$

where α is the wall expansion ratio defined as

$$\alpha(t) = \dot{a}a / \nu \tag{21}$$

Note that allowing $p_{xy} = 0$ in Eq. (2) will also lend itself as a method of arriving at Eq. (20). The boundary conditions given by Eqs. (4)-(5) can be now updated to account for the normalization. One finds

$$\begin{cases} F_{\eta\eta} = 0 & F = 0 & \eta = 0 \\ F_{\eta} = 0 & F = A\alpha = R & \eta = 1 \end{cases} \tag{22}$$

B. Similar Solution in Space and Time

A similar solution with respect to space and time can now be developed. If our function F is made dependent on η and $\alpha(t)$ instead of (η, t), then one obtains $F_{\eta t} = 0$ by setting α to be constant or quasi-constant in time. In that event, the value of the expansion ratio α can be specified by its initial value viz.

$$\alpha = \dot{a}a / \nu = \dot{a}_0 a_0 / \nu \tag{23}$$

where a_0 and $\dot{a}_0 = \mathrm{d}a_0 / \mathrm{d}t$ denote the initial channel height and channel expansion ratio, respectively. By integrating Eq. (23) with respect to time, a similar solution for the temporal channel height evolution can be obtained. This is given by

$$a(t) / a_0 = \left(1 + 2\nu\alpha t a_0^{-2}\right)^{\frac{1}{2}} \tag{24}$$

For a physical setting in which the injection coefficient A is constant (e.g., propellant burning), an expression for the time-dependent injection velocity evolution can be deduced. One gets

$$\dot{a} / \dot{a}_0 = v_{\mathrm{w}}(t) / v_{\mathrm{w}}(0) = \left(1 + 2\nu\alpha t a_0^{-2}\right)^{-\frac{1}{2}} \tag{25}$$

Under the foregoing self-similarity conditions, an ODE for the principal function F can be derived by direct integration of Eq. (20). One obtains

$$F''' + FF'' + F'\left(2\alpha - F'\right) + \alpha\eta F'' = K \tag{26}$$

where a prime replaces $\mathrm{d} / \mathrm{d}\eta$ and K is the constant of integration. The necessary boundary conditions translate into

$$\begin{cases} F'' = 0 & F = 0 & \eta = 0 \\ F' = 0 & F = R & \eta = 1 \end{cases} \tag{27}$$

C. Numerical Solution

Since the problem exhibits four boundary conditions, it is convenient to eliminate the integration constant K by differentiating Eq. (26) with respect to η. The resulting governing ODE becomes

$$F^{IV} + FF''' + F''\left(3\alpha - F'\right) + \alpha\eta F''' = 0 \tag{28}$$

Equation (28) can be solved numerically by applying a shooting method coupled with fourth-order Runge-Kutta integration. The procedure used to obtain the function F is described next.

1. Shooting Method

The boundary conditions for Eq. (28) can be restated as

$$\begin{aligned} F''(0) &= 0 & F(0) &= 0 \\ F'''(0) &= \kappa & F'(0) &= \tau \\ F'(1) &= 0 & F(1) &= R \end{aligned} \tag{29}$$

where τ and κ are the initial guesses on which the solution strongly depends. At the outset, one can express Eq. (28) in the classic form

$$y^{IV} = f\left(x, y, y', y'', y'''\right) = y''\left(y' - 3\alpha\right) - yy''' - \alpha x y''' \tag{30}$$

where the function $y(x) \equiv F(\eta)$ in this section should not be mistaken for the normal coordinate y in dimensional form. Thereupon,

$$f = y''\left(y' - 3\alpha\right) - yy''' - \alpha x y''' . \tag{31}$$

In like fashion, the boundary conditions become

$$\begin{aligned} y'''(0) &= \kappa & y''(0) &= 0 \\ y'(0) &= \tau & y(0) &= 0 \end{aligned} \tag{32}$$

To satisfy the endpoint boundary conditions at $\eta = 1$, the functions $g(\tau, \kappa)$ and $h(\tau, \kappa)$ are introduced such that

$$\begin{aligned} g(\tau, \kappa) &= y(1, \tau, \kappa) - R = 0 \\ h(\tau, \kappa) &= y'(1, \tau, \kappa) - 0 = 0 \end{aligned} \tag{33}$$

Based on Newton's generalized method, an algorithm for calculating the zeros τ^* and κ^* of Eq. (33) can be implemented. The algorithm requires updating initial guesses following

$$\begin{bmatrix} \tau \\ \kappa \end{bmatrix}_{n+1} = \begin{bmatrix} \tau \\ \kappa \end{bmatrix}_{n} - [J]^{-1} \cdot \begin{bmatrix} y(1, \tau, \kappa) - R \\ y'(1, \tau, \kappa) \end{bmatrix}_{n} \tag{34}$$

where n is the iteration index and $[J]^{-1}$ is the inverse of the Jacobian matrix.

At this point, two new functions T and K can be posited such that

$$\mathrm{T}(x,\tau,\kappa) \equiv \frac{\partial y}{\partial \tau} \text{ and } \mathrm{K}(x,\tau,\kappa) \equiv \frac{\partial y}{\partial \kappa} \tag{35}$$

Following this transformation, the boundary conditions can be determined as illustrated in the following example for $\mathrm{T}_x(0,\tau,\kappa)$. Starting with

$$\mathrm{T}_x = \frac{\partial}{\partial x}\left(\frac{\partial y}{\partial \tau}\right) = \frac{\partial}{\partial \tau}\left(\frac{\partial y}{\partial x}\right)$$

one can then evaluate the function at the endpoint,

$$\mathrm{T}_x(0,\tau,\kappa) = \frac{\partial}{\partial \tau}\left[y'(0)\right] = \frac{\partial}{\partial \tau}[\tau] = 1 \tag{36}$$

Likewise, the boundary conditions for T and K in Eq. (31) become

$$\begin{aligned} &\mathrm{T}(0,\tau,\kappa) = 0 && \mathrm{K}(0,\tau,\kappa) = 0 \\ &\mathrm{T}_x(0,\tau,\kappa) = 1 && \mathrm{K}_x(0,\tau,\kappa) = 0 \\ &\mathrm{T}_{xx}(0,\tau,\kappa) = 0 && \mathrm{K}_{xx}(0,\tau,\kappa) = 0 \\ &\mathrm{T}_{xxx}(0,\tau,\kappa) = 0 && \mathrm{K}_{xxx}(0,\tau,\kappa) = 0 \end{aligned} \tag{37}$$

Next, the order of differentiation in Eq. (30) can be switched such that

$$\frac{\partial f}{\partial \tau} = \frac{\partial\left(y_{xxxx}\right)}{\partial \tau} = \frac{\partial^4}{\partial x^4}\left(\frac{\partial y}{\partial \tau}\right) \tag{38}$$

Since $\mathrm{T} = \partial y / \partial \tau$, a fourth-order differential equation for T can be written in the form

$$\mathrm{T}^{IV} = f_y \mathrm{T} + f_{y'} \mathrm{T}' + f_{y''} \mathrm{T}'' + f_{y'''} \mathrm{T}''' \tag{39}$$

whose boundary conditions are given by Eq. (37). A similar expression involving K is found to be

$$\mathrm{K}^{IV} = f_y \mathrm{K} + f_{y'} \mathrm{K}' + f_{y''} \mathrm{K}'' + f_{y'''} \mathrm{K}''' \tag{40}$$

with the same boundary conditions listed in Eq. (37).

Returning to Newton's generalized method that is needed to solve for the correct initial guesses, one must first define the Jacobian matrix via

$$J = \begin{bmatrix} \partial f_1 / \partial \tau & \partial f_1 / \partial \kappa \\ \partial f_2 / \partial \tau & \partial f_2 / \partial \kappa \end{bmatrix} \qquad \begin{aligned} f_1 &= y - R \\ f_2 &= y' \end{aligned} \tag{41}$$

which, in this problem, simplifies to:

$$J = \begin{bmatrix} \mathrm{T}(1) & \mathrm{K}(1) \\ \mathrm{T}_x(1) & \mathrm{K}_x(1) \end{bmatrix} \tag{42}$$

Once the inverse of the Jacobian in Eq. (42) is determined, Eq. (34) reduces to

$$\begin{bmatrix} \tau \\ \kappa \end{bmatrix}_{n+1} = \begin{bmatrix} \tau \\ \kappa \end{bmatrix}_n - c \begin{bmatrix} \mathrm{K}_x & -\mathrm{K} \\ -\mathrm{T}_x & \mathrm{T} \end{bmatrix} \begin{bmatrix} y - R \\ y' \end{bmatrix}_n \tag{43}$$

where $c = 1/\det(J) = [\mathrm{T}(1)\mathrm{K}_x(1) - \mathrm{K}(1)\mathrm{T}_x(1)]^{-1}$

2. Runge-Kutta Solution Method

The shooting method described above was chosen for its ease of conversion into a ready-to-integrate Runge-Kutta solution set. Twelve variables are chosen to represent y, T, K, and their respective derivatives out to the third order. Differentiating each of these functions and performing the appropriate substitutions provides a convenient solution set. The Runge-Kutta method is an effective approach in this application since it enables us to enter the prescribed boundary conditions only once for all twelve variables. The solution also requires the input of initial guesses for the boundary condition values of τ and κ which are then iterated according to

$$\begin{aligned} \tau_{n+1} &= \tau_n + \frac{\mathrm{K}(1)\,y'(1) + \mathrm{K}_x(1)[R - y(1)]}{\mathrm{T}(1)\mathrm{K}_x(1) - \mathrm{K}(1)\mathrm{T}_x(1)} \\ \kappa_{n+1} &= \kappa_n + \frac{\mathrm{T}_x(1)[y(1) - R] - \mathrm{T}(1)\,y'(1)}{\mathrm{T}(1)\mathrm{K}_x(1) - \mathrm{K}(1)\mathrm{T}_x(1)} \end{aligned} \tag{44}$$

IV. Flow-Field Characterization

A. Non-dimensional Variables

Once we obtain a numerical solution for F, the dimensionless stream function and velocity components become available. The stream function can be normalized by its value at the wall ($\eta = 1$) in view of Eq. (27); letting $\psi(1) = \nu x F(1)/a = \nu x R/a$, we then write

$$\psi^* \equiv \frac{\psi}{\psi(1)} = \frac{F}{R} \tag{45}$$

In view of Eq. (18) and Eq. (11), the axial velocity can be normalized by the mean axial velocity such that

$$u^* = \frac{u}{u_{\mathrm{m}}} = \frac{F'}{R} \tag{46}$$

independently of the axial position. Profiles of u^* can then be displayed for small, moderate, and large injection and suction in Figs. 2 and 3, respectively.

Finally, since the velocity at the wall may be expressed as $v(1) = -v_{\mathrm{w}} = -\nu R/a$, the normal velocity may be referenced to the value at the wall such that

$$v^* = \frac{v}{v(1)} = \frac{\psi}{\psi(1)} = \frac{F}{R} \tag{47}$$

The normalized stream function and normal velocity components are therefore identical and can be illustrated in Fig. 4 for both small-to-moderate injection and suction.

B. Pressure and Shear Distributions

To complete our flow-field analysis, the resulting pressure gradients and shear stress distributions are considered as well. An expression for the normal pressure gradient can be developed by substituting the velocity components of Eq. (18) into Eq. (3) with F acting as a function of η only. The result is

$$p_\eta = -\nu^2 \rho a^{-2}\left[F_{\eta\eta} + F F_\eta + \alpha\left(F + \eta F_\eta\right)\right] \tag{48}$$

The normal pressure distribution is found by manipulating Eq. (48) before integrating and applying the boundary conditions of Eq. (27). Proceeding by writing

$$\int_{p(x,0)}^{p(x,\eta)} \mathrm{d}p = \int_0^{\eta} -\frac{\rho\nu^2}{a^2}\left[F_{\eta\eta} + FF_{\eta} + \alpha\left(F + \eta F_{\eta}\right)\right]\mathrm{d}\eta \tag{49}$$

the pressure distribution in the normal direction can be non-dimensionalized and written as

$$p_{\mathrm{n}}{}^{*} = \frac{p(x,\eta) - p(x,0)}{\rho\nu^2 / a^2} = F_{\eta}(0) - \left(\alpha\eta F + \tfrac{1}{2}F^2 + F_{\eta}\right) \tag{50}$$

The normal pressure drop $p_{\mathrm{n}}{}^{*}$ can now be shown in Fig. 5 over a range of α and R.

Since F behaves as a function of η only and $F_{\eta t} = 0$ in the axial direction, substitution of the velocity components from Eq. (18) into the axial momentum Eq. (2) yields the axial pressure gradient:

$$\frac{\partial p}{\partial x} = \frac{\rho\nu^2 x}{a^4}\left[F''' + FF'' + F'\left(2\alpha - F'\right) + \alpha y F''\right] \tag{51}$$

In light of Eq. (26), Eq. (51) can be simplified into

$$\frac{\partial p}{\partial x} = \frac{\rho\nu^2 x}{a^4}K \tag{52}$$

This can be readily integrated and non-dimensionalized to obtain the axial pressure distribution at any axial position:

$$p_{\mathrm{a}}{}^{*} = \frac{p(x,\eta) - p(0,\eta)}{\rho\nu^2 / a^2}\frac{a^2}{a_0^2} = \frac{K}{2}\frac{x^2}{a_0^2} \tag{53}$$

The axial pressure drop $p_{\mathrm{a}}{}^{*}$ can be described in Fig. 6 by plotting it over a range of α and R.

Finally, the shear stress due to flow past the porous surface can be determined from Newton's law for viscosity, namely,

$$\tau = \mu\left(\frac{\partial u}{\partial y} + \frac{\partial v}{\partial x}\right) \tag{54}$$

Thus, by substituting the velocity components from Eq. (18) into the shear stress equation, one may non-dimensionalize after expressing the results at the wall. One finds

$$\tau^{*} = \frac{\tau_{\mathrm{w}}}{\rho\nu^2 / a_0^2}\frac{a^3}{a_0^3} = \frac{x}{a_0}F''(1) \tag{55}$$

where τ^{*} represents the dimensionless stress at the wall. The shear stress can be described in Fig. 7 by plotting it over a range of α and R.

V. Results

In an effort to develop a better understanding of the effects of viscosity and wall deformation on the flow character, the main flow attributes are described over different ranges of the control parameters R and α. This additional insight into the physics of the problem may be achieved through a detailed interpretation of the axial and normal velocities, axial and normal pressure distributions, shear stress at the wall, and the streamline behavior.

A. Axial Velocity

Figure 2 illustrates the behavior of the axial velocity profiles for low, moderate, and high injection Reynolds numbers taken over a range of wall expansion/contraction scenarios. An initial glance indicates the greater sensitivity to wall regression at the low injection case of $R = 5$ (Fig. 2a). This phenomenon manifests itself in the form of flow reversal that is most clearly depicted in the $R = 5$, $\alpha = 100$ case. Therein, the rate of expansion is very large compared to the rate of mass addition at the boundaries. The rapid volumetric expansion of the

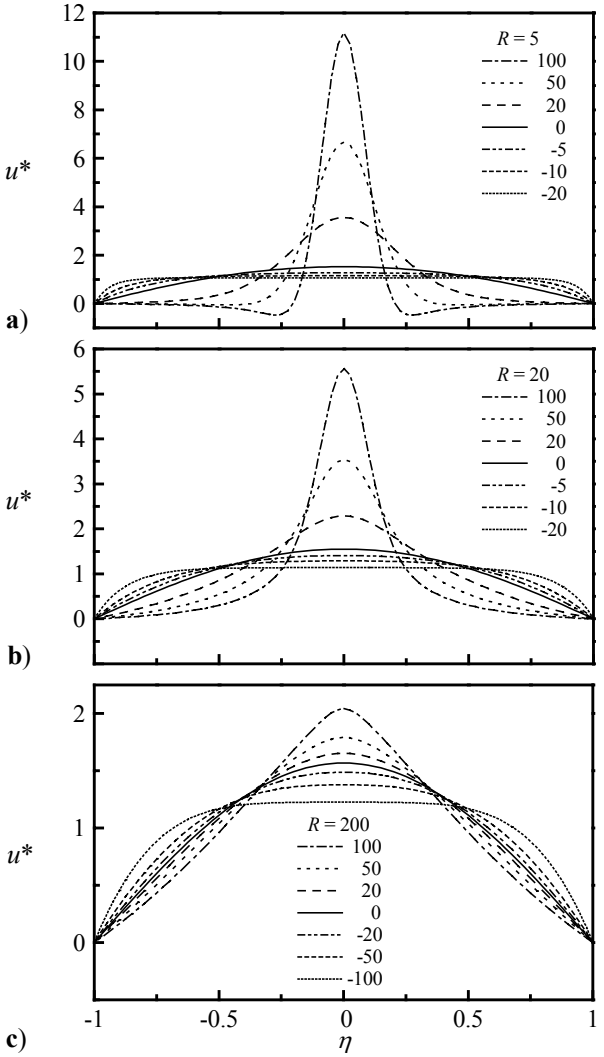

Fig. 2. Axial velocity profiles shown over a range of wall expansion (or contraction) ratios and an injection Reynolds number of a) 5, b) 20, and c) 200.

walls creates suction regions near the closed head-end where a mass deficiency is suddenly formed. The incompressible fluid is thus forced upstream in the head-end direction in order to occupy the space accompanying the expansion process. The same fluid has to later turn and head downstream towards the open end. It should be noted that flow reversal seems to occur, in all cases, when the relative injection ratio, $|\alpha / R|$, exceeds the value of 10. As such, the $R = 5$, $\alpha = 50$ case may be seen, in Fig. 2a, to delimit the borderline beyond which flow reverses.

If the injection is large enough, however, Figs. 2b–c indicate that flow reversal can be suppressed. Under such circumstances, the fluid that enters the channel can rapidly fill the gap created by the moving walls in a manner to preclude flow reversal. Note, in particular, the $R = 20$, $\alpha = 100$ case in Fig. 2b where the flow is at the verge of flow reversal. Such a situation can arise when the moderate injection Reynolds number is able to compensate for the rapid wall expansion rate. The absence of flow reversal is also consistent with the criterion that we have set earlier because the relative expansion to injection ratio in the case at hand happens to be $|\alpha / R| = 5 < 10$. For added clarity, the injection-driven streamlines are furnished in Figs. 8a–c.

It may be interesting to note the special case of stationary walls at $\alpha = 0$ where the centerline-to-mean velocity ratio, $u^*(0)$, is equal to $3/2$. This value matches the centerline-to-mean velocity ratio in the fully-developed Hagen-Poiseuille flow whose profile is that of a parabolic cylinder extending across the width of the channel.

Figure 3 presents the axial velocity profiles that occur for low, moderate, and high suction Reynolds numbers. Here too, a flow reversal mechanism that is similar to that described for injection can take place. In fact, flow reversal can be seen in Figs. 3a and 3c, for the $R = -1$, $\alpha = 10, 5$, and $R = -50$, $\alpha = 50$ cases. In all cases, the relative suction ratio $|\alpha / R| \geq 1$. In fact, it appears that flow reversal begins when the expansion to suction ratio exceeds 1. Since the volumetric expansion rate is appreciable in comparison to the fluid withdrawal rate, the inception of suction regions near the head-end causes the fluid to move farther upstream to occupy the rapidly created space near the closed end. The same fluid that has moved upstream has to later swerve and head downstream towards the suction sites along the porous surface. This behavior can be clearly seen in Fig. 8d–f where flow streamlines are shown.

For increasing suction, one observes in Figs. 3b–c that the velocity profiles gradually become more flat while asymptoting to a spatially uniform value. The flattening in the profile is, of course, indicative of

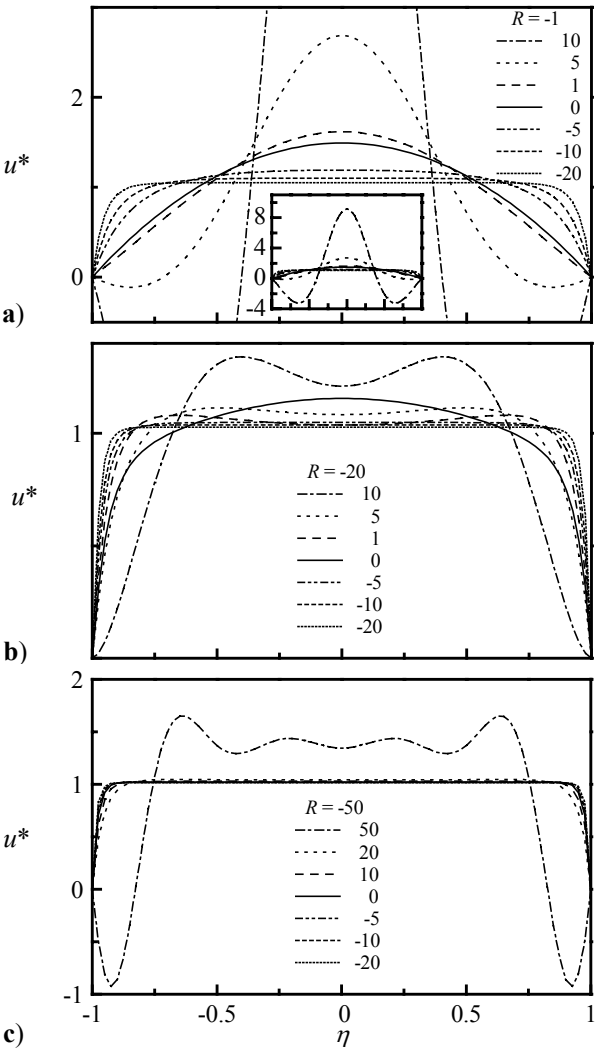

Fig. 3. Axial velocity profiles shown over a range of wall expansion ratios and a suction Reynolds number of a) -1, b) -20, and c) -50.

thinning boundary layers. This is consistent with classic laminar flow theory. In this problem, a sufficiently large suction can dominate over wall expansion and attracts the boundary layer closer to the walls.

Increasing wall contraction, on the other hand, causes the profile to level off more rapidly so that $u^*(0) \to 1$ at lower values of suction. This phenomenon is clearly seen in Figs. 3a–c for $\alpha < 0$. As such, one may conceive of an effective suction Reynolds number, $R_s = -(R + \alpha)$ that combines the convective effects of with the wall motion. By running multiple tests, we find that as R_s increases beyond 20, the flow approaches the inviscid flow solution that exists for infinitely large suction.

B. Normal Velocity

The behavior of the normal velocity is illustrated in Figure 4. Four different values of the cross flow Reynolds number are presented on two sets of axes for purposes of compactness and ease of comparison. Two interesting phenomena can be observed from these velocity profiles. The first corresponds to the existence of a point on the interval $-1 < \eta < 0$ where the normal velocity exceeds its (absolute) value at the wall. This is, again, most noticeable in the low injection and suction cases (left halves of Figures 4a and b) experiencing flow reversal. This occurs during rapid wall expansions and contractions leading to $|\alpha / R|$ in excess of 10 for injection (Fig. 4a), and 1 for suction (Fig. 4b). For the scenario of low flow injection into a rapidly expanding channel in Fig. 4a, the point of maximum normal velocity moves away from the wall in order to satisfy mass conservation. As the injected flow turns towards the head-end, it collides with the incoming stream along the upstream sections of the porous surface. The causes the normal velocity to overshoot above its value at the wall in order to compensate for a larger influx per unit area. The radial velocity overshoot seen in Fig. 4 can be attributed to the presence of flow reversal and collision regions. These so-called collision regions have been observed in other studies by Brady[24] and Brady and Acrivos.[13]

The second interesting point is that the solutions to the moderate injection and suction cases all tend to the same respective curve with increasing Reynolds numbers. As $|R|$ increases in the injection case, the relative importance of α diminishes; and ultimately, $|\alpha / R|$ becomes sufficiently small, regardless of the expansion/contraction value. For $|\alpha / R| < 0.1$, the dimensionless velocity becomes indistinguishable from the inviscid Taylor profile given by $\sin(\frac{1}{2}\pi\eta)$.[7]

In the suction case, however, one needs to measure the effective suction Reynolds number, R_s. As R_s is successively increased above 20, the normal suction velocity becomes increasingly more linear. It approaches its expected value of $v^* = \eta$ for an inviscid suction flow.[2,3] For this reason, large injection or suction cases are not always shown whenever the corresponding curves are found to cluster very near the inviscid solution.

C. Normal and Axial Pressure Distributions

Figure 5 exhibits the normal pressure drop of low and moderate values of the cross flow Reynolds number for various expansion/contraction cases. For every level of injection or suction save one, the absolute pressure change is at its largest near the wall. The deviate to this trend is the scenario involving low suction with a

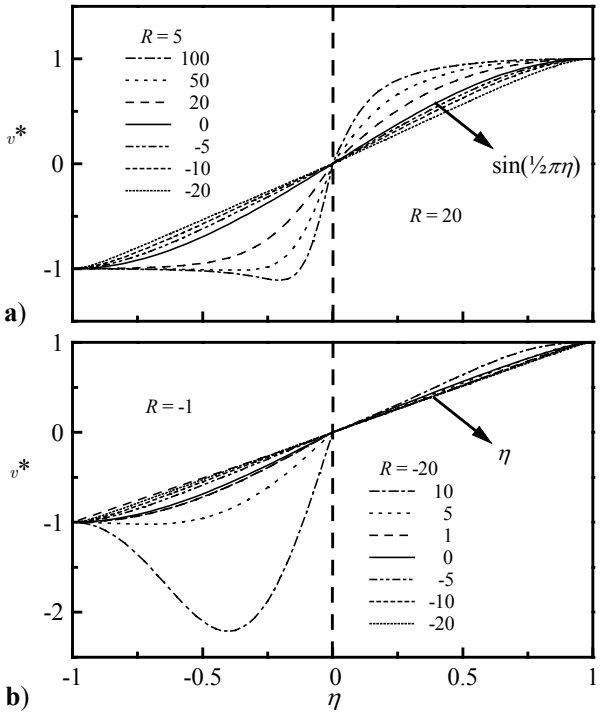

Fig. 4. Normal velocity profiles shown over a range of expansion ratios and crossflow Reynolds numbers corresponding to a) injection, and b) suction.

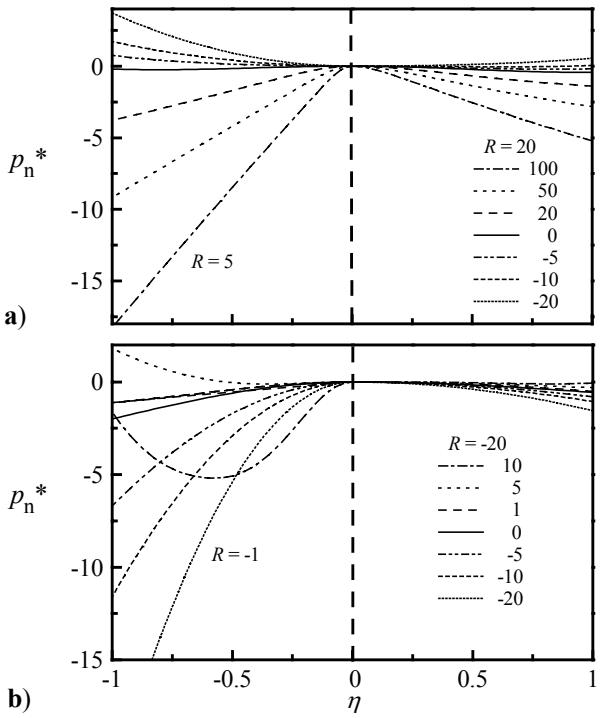

Fig. 5. Normal pressure drop shown over a range of expansion ratios and crossflow Reynolds numbers corresponding to a) injection, and b) suction.

rapidly expanding channel ($R=-1$ at $\alpha=10$). Referring back to the axial velocity profile for this particular case, as shown Fig. 3a, one can observe that appreciable flow reversal accompanies the unique behavior implied by the set of governing parameters.
Moving on, one may also note that, in general, increasing the rate of wall contraction during injection increases the pressure drop. Increasing the expansion rate during suction also increases the pressure drop until flow reversal occurs. For an injection/expansion process, or a suction/contraction process, the pressure drop diminishes with the successive increases in $|\alpha|$.

The parabolic behavior of the axial pressure distribution is captured in Figure 6. One may begin by noting that the higher the wall contraction rate is, the greater the absolute pressure change will be. That is, the absolute pressure drop is reduced as $|\alpha|$ is diminished. Moreover, one notes that the pressure drop is typically favorable (i.e., negative) for injection with contraction; however, when expansion becomes sufficiently large, flow reversal takes place and the pressure drop switches signs (see $R=20$ and $\alpha=100$). For a suction-driven process, the converse is true. For a suction/contraction process, the pressure drop is favorable (positive for the suction flow). It can turn to adverse (negative) when the expansion rate becomes sufficiently large (see $R=-20$ and $\alpha=10$). The adverse pressure drops are consistent with the criteria established above.

D. Wall Shear Stress Distribution

Figure 7 illustrates the effects of varying the governing parameters on the character of the shear stress at the wall. For the same physical reasons, the trends accompanying the shear stress are identical to those associated with the axial pressure behavior. On that account, an injection/contraction process leads to a negative (favorable) shear stress that opposes the primary direction of motion. However, when expansion increases beyond a certain level, flow reversal occurs and the shear stress turns slightly positive (e.g., $R=20$ and $\alpha=100$). That condition is established when the flow injected moves to the head-end first, before turning downstream. For a suction/contraction process, the shear stress is positive (favorable) until expansion is sufficiently large. For example, when $R=-20$ and $\alpha=5,10$ in Fig. 7b, the shear stress turns negative owing to flow reversal. For the cases of suction in Fig. 6b, we observe that the shear stress at the wall increases as the contraction ratio $|\alpha|$ is increased. This can be attributed to the increased skin friction associated with rapid wall motion in comparison with the stationary wall case. In the latter, the shear stress variation is typically small, increases in the downstream direction, and becomes larger at higher

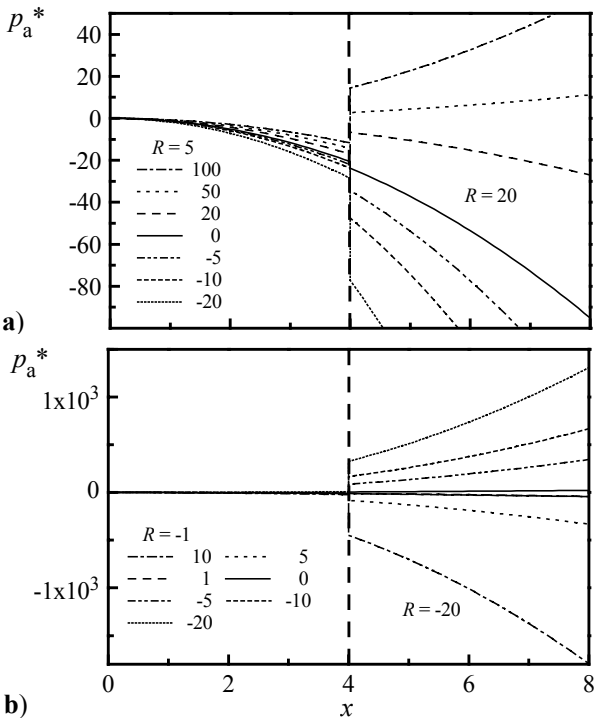

Fig. 6. Axial pressure drop over a range of α and R corresponding to a) injection, and b) suction.

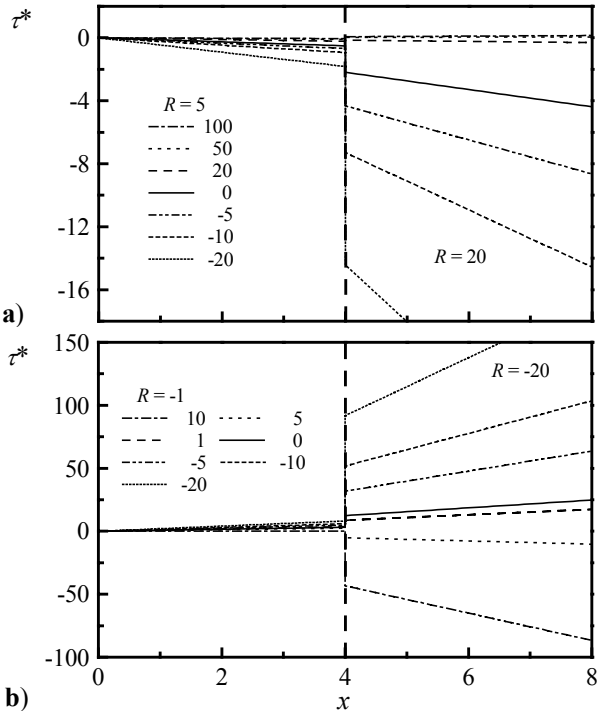

Fig. 7. Same as previous for wall shear stress.

suction rates (due thinning boundary layers and steeper slopes at the wall).

E. Streamlines

Streamlines originating or terminating at several discrete points along the length of the wall are presented in Figure 8 over a wide range of cross flow Reynolds numbers and expansion ratios. We can clearly see that injection tends to push the streamlines closer to the core while suction draws them somewhat away from the core and closer to the wall. In the same vein, large suction promotes a more abrupt change in the flow direction from axial to normal. This tends to be accompanied by sharper flow turning near the wall. Conversely, cases rapidly expanding walls will experience delayed flow turning and flow reversal–as hinted at earlier. These differences in streamline curvature, and hence, the flow turning rate, become more appreciable when we focus our attention further downstream. Thus, the effects of viscosity are more significant in the downstream portions of the channel.

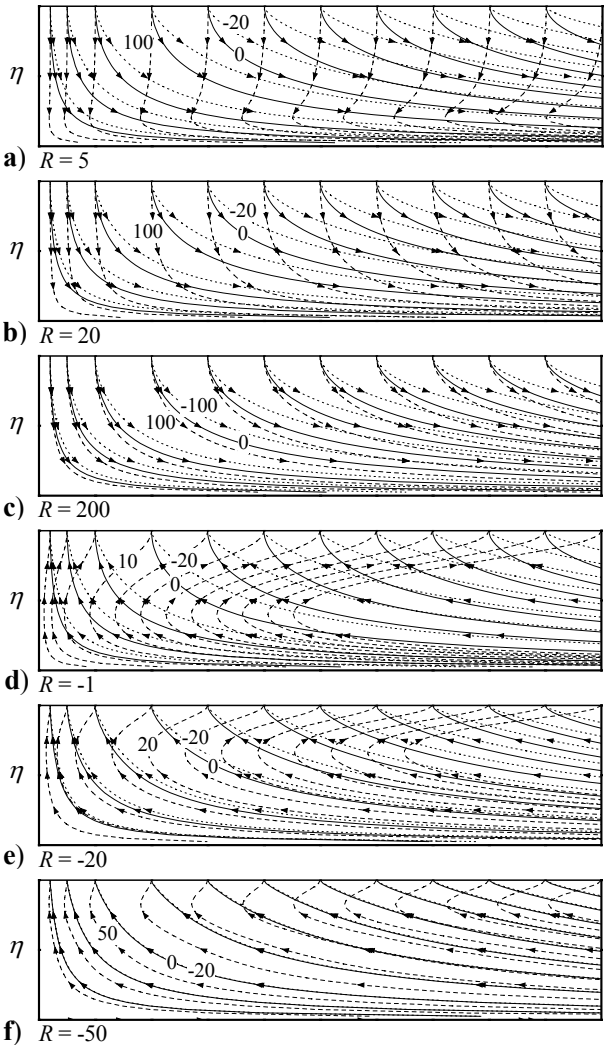

Fig. 8. Flow streamlines shown over a range of expansion ratios and crossflow Reynolds numbers.

In turning our attention to the effects of α, we observe that the higher the expansion speed, the longer the normal velocity will be large in comparison to its axial counterpart while approaching the core. One can then imagine a purely hypothetical scenario where the walls expand at nearly the same speed as that of the fluid entering the channel. Thus, when $\dot{a} = v_b$, the expansion process offsets the effect of injection to the point that streamlines will exhibit an infinite radius of curvature and remain perpendicular to the walls. If this situation occurs, the flow turning will be delayed indefinitely with the cessation of downstream motion.

VI. Conclusions

The current analysis presents a procedure that establishes an exact similarity solution of the Navier-Stokes equations in semi-infinite rectangular channels with porous and uniformly expanding walls. It is found that in rectangular chambers and ducts where wall regression and injection occur simultaneously, the streamlines, pressure distributions, and shear stresses are time and space dependent. They can be characterized by two dimensionless parameters: the expansion ratio of the walls α and the cross-flow Reynolds number *R*. A shooting method, coupled with a Runge-Kutta integration scheme, were utilized to numerically solve the fourth order differential equation. The results contributed to further explain the physics behind the flow-field character. In summary, interesting structures were observed including the formation of collision regions where flow reverses near the head-end section of the channel. These collision regions are typically found when the relative expansion ratio is large, namely,

$$|\alpha / R| \geq \begin{cases} 10, & \text{injection} \\ 1, & \text{suction} \end{cases} \tag{56}$$

On the other hand, for sufficiently large $|R|$, solutions are found to asymptote to the inviscid-flow analogue in a porous channel for which Taylor's sinusoidal profile for injection,[7] or Sellars' linear profile for suction become suitable approximations.[2] In fact, results become hardly distinguishable when

$$|\alpha / R| < 0.1 \tag{57}$$

for injection. For suction, the criterion must be based on the effective Reynolds number, $R_s = -(R + \alpha)$. Accordingly, the current solution will resemble Sellar's inviscid profile for $R_s > 20$. These criteria extend our understanding of laminar flows in porous channels. We hope, in a forthcoming study, to address the onset and evolution of flow instability.

References

[1]Berman, A. S., "Laminar Flow in Channels with Porous Walls," *Journal of Applied Physics,* Vol. 24, No. 9, 1953, pp. 1232-1235.

[2]Sellars, J. R., "Laminar Flow in Channels with Porous Walls at High Suction Reynolds Numbers," *Journal of Applied Physics,* Vol. 26, No. 4, 1955, pp. 489-490.

[3]Terrill, R. M., "Laminar Flow in a Uniformly Porous Channel," *The Aeronautical Quarterly,* Vol. 15, 1964, pp. 299-310.

[4]Proudman, I., "An Example of Steady Laminar Flow at Large Reynolds Number," *Journal of Fluid Mechanics,* Vol. 9, No. 4, 1960, pp. 593-612.

[5]Morduchow, M., "On Laminar Flow through a Channel or Tube with Injection: Application of Method of Averages," *Quarterly Journal of Applied Mathematics,* Vol. 14, No. 4, 1957, pp. 361-368.

[6]White, F. M., Jr., Barfield, B. F., and Goglia, M. J., "Laminar Flow in a Uniformly Porous Channel," *Transactions of the American Society of Mechanical Engineers: Journal of Applied Mechanics, Series E,* Vol. 25, 1958, pp. 613-617.

[7]Taylor, G. I., "Fluid Flow in Regions Bounded by Porous Surfaces," *Proceedings of the Royal Society, London, Series A,* Vol. 234, No. 1199, 1956, pp. 456-475.

[8]Yuan, S. W., "Further Investigation of Laminar Flow in Channels with Porous Walls," *Journal of Applied Physics,* Vol. 27, No. 3, 1956, pp. 267-269.

[9]Terrill, R. M., "Laminar Flow in a Uniformly Porous Channel with Large Injection," *The Aeronautical Quarterly,* Vol. 16, 1965, pp. 323-332.

[10]Terrill, R. M., and Shrestha, G. M., "Laminar Flow through Parallel and Uniformly Porous Walls of Different Permeability," *Journal of Applied Mathematics and Physics (ZAMP),* Vol. 16, 1965, pp. 470-482.

[11]Shrestha, G. M., and Terrill, R. M., "Laminar Flow with Large Injection through Parallel and Uniformly Porous Walls of Different Permeability," *Quarterly Journal of Mechanics and Applied Mathematics,* Vol. 21, No. 4, 1968, pp. 413-432.

[12]Cox, S. M., "Two-Dimensional Flow of a Viscous Fluid in a Channel with Porous Walls," *Journal of Fluid Mechanics,* Vol. 227, 1991, pp. 1-33.

[13]Brady, J. F., and Acrivos, A., "Steady Flow in a Channel or Tube with an Accelerating Surface Velocity. An Exact Solution to the Navier-Stokes Equations with Reverse Flow," *Journal of Fluid Mechanics,* Vol. 112, 1981, pp. 127-150.

[14]Watson, E. B. B., Banks, W. H. H., Zaturska, M. B., and Drazin, P. G., "On Transition to Chaos in Two-Dimensional Channel Flow Symmetrically Driven by Accelerating Walls," *Journal of Fluid Mechanics,* Vol. 212, 1990, pp. 451-485.

[15]Watson, P., Banks, W. H. H., Zaturska, M. B., and Drazin, P. G., "Laminar Channel Flow Driven by Accelerating Walls," *European Journal of Applied Mathematics,* Vol. 2, 1991, pp. 359-385.

[16]Varapaev, V. N., and Yagodkin, V. I., "Flow Stability in a Channel with Porous Walls," *Fluid Dynamics (Izvestiya Akademii Nauk SSSR, Meckanika Zhidkosti i Gaza),* Vol. 4, No. 5, 1969, pp. 91-95.

[17]Raithby, G. D., and Knudsen, D. C., "Hydrodynamic Development in a Duct with Suction and Blowing," *Transactions of the American Society of Mechanical Engineers: Journal of Applied Mechanics, Series E,* Vol. 41, 1974, pp. 896-902.

[18]Sviridenkov, A. A., and Yagodkin, V. I., "Flow in the Initial Sections of Channels with Permeable Walls," *Fluid Dynamics (Izvestiya Akademii Nauk SSSR, Meckanika Zhidkosti i Gaza),* Vol. 11, No. 5, 1976, pp. 689-693.

[19]Ma, Y., Van Moorhem, W. K., and Shorthill, R. W., "Innovative Method of Investigating the Role of Turbulence in the Velocity Coupling Phenomenon," *Journal of Vibration and Acoustics-Transactions of the ASME,* Vol. 112, No. 4, 1990, pp. 550-555.

[20]Ma, Y., Van Moorhem, W. K., and Shorthill, R. W., "Experimental Investigation of Velocity Coupling in Combustion Instability," *Journal of Propulsion and Power,* Vol. 7, No. 5, 1991, pp. 692-699.

[21]Barron, J., Majdalani, J., and Van Moorhem, W. K., "A Novel Investigation of the Oscillatory Field over a Transpiring Surface," AIAA Paper 98-2694, June 1998.

[22]Goto, M., and Uchida, S., "Unsteady Flows in a Semi-Infinite Expanding Pipe with Injection through Wall," *Transactions of the Japan Society for Aeronautical and Space Sciences,* Vol. 33, No. 9, 1990, pp. 14-27.

[23]Uchida, S., and Aoki, H., "Unsteady Flows in a Semi-Infinite Contracting or Expanding Pipe," *Journal of Fluid Mechanics,* Vol. 82, No. 2, 1977, pp. 371-387.

[24]Brady, J. F., "Flow Development in a Porous Channel or Tube," *The Physics of Fluids,* Vol. 27, No. 5, 1984, pp. 1061-1067.